Journal of MATERIALS RESEARCH

Article
DOI: 10.1557/jmr.2020.97

HETEROGENEITY IN 2D MATERIALS

FOCUS ISSUE

Hydrothermal synthesis of carbon nanotube–titania composites for enhanced photocatalytic performance

Brian M. Everhart[1], Montgomery Baker-Fales[1], Bailey McAuley[1], Eric Banning[1], Haider Almkhelfe[1], Tyson C. Back[2], Placidus B. Amama[1,a)]

[1]Tim Taylor Department of Chemical Engineering, Kansas State University, Manhattan, Kansas 66506, USA
[2]Materials and Manufacturing Directorate, Air Force Research Laboratory, WPAFB, Ohio 45433, USA
[a)]Address all correspondence to this author. e-mail: pamama@ksu.edu

Received: 20 December 2019; accepted: 31 March 2020

Nanosized, well-dispersed titania particles were synthesized via a hydrothermal method using multiwalled carbon nanotubes (MWCNTs) as structural modifiers during the nucleation process to decrease aggregation. Synthesized TiO_2/MWCNT composites containing different amounts of MWCNTs were characterized using N_2 physisorption, XRD, spectroscopic techniques (Raman, UV-visible, and X-ray photoelectron), and electron microscopy to illuminate the morphology, crystal structure, and surface chemistry of the composites. Photocatalytic performance was evaluated by measuring the degradation of acetaldehyde in a batch reactor under UV illumination. Average rate constants decrease in the following order: TiO_2/MWCNT-1% > TiO_2 > TiO_2/MWCNT-5%. Addition of MWCNTs beyond the optimum loading ratio of 1:100 (MWCNT:TiO_2) diminishes the effectiveness of the photocatalyst and the synergistic effect between MWCNTs and TiO_2. The primary mechanism for photocatalytic activity enhancement in TiO_2/MWCNT-1% is thought to be due to increased porosity, hydroxyl enrichment on the surface, and high dispersion of TiO_2 particles.

Introduction

Photocatalytic oxidation (PCO) using semiconductors as catalysts has become an appealing approach as a green technology for environmental remediation since the discovery of UV-assisted splitting of water on TiO_2 by Fujishima and Honda [1]. Air contaminants such as SO_x, NO_x, halogenated organics, and volatile organic compounds (VOCs) are suitable candidates for PCO [2, 3, 4, 5, 6, 7, 8, 9, 10]. TiO_2 has been identified as the most promising photocatalytic material based on its strong oxidizing power, chemical stability, relatively low price, and biological benignity [11, 12]. However, photocatalytic performance of conventional TiO_2 is limited by its wide band gap (3.2 eV for the anatase crystal phase [13]) and fast electron–hole recombination. These properties restrict the photon absorption range to ultraviolet wavelengths (only 8.3% of total solar irradiance [14]) and limit the quantum efficiency [15, 16].

In an effort to overcome these problems and increase the photocatalytic activity of TiO_2, researchers have explored a number of modification approaches [17, 18, 19, 20] and recently turned to carbon nanotubes (CNTs) and other carbon nanomaterials [21, 22, 23, 24]. CNTs, which are either single-walled (SWCNTs) or multiwalled (MWCNTs), possess unique properties that make them the ideal supports for catalysts such as large surface area (>200 m^2/g), high thermal and chemical stability, as well as excellent electrical and mechanical properties. In particular, CNTs have a large electron-storage capacity (one electron for every 32 carbon atoms) and thus can serve as an electron sink; in addition, the highly conductive nature of CNTs promotes charge separation via the creation of heterojunctions at the CNT–TiO_2 interface [25]. A number of studies [21, 22, 23, 24, 25, 26, 27, 28, 29, 30, 31] have shown the unique electronic properties of CNTs can be exploited to induce beneficial charge transfer properties and synergistic effects between carbon phases and TiO_2; thus coupling CNTs to TiO_2 can improve the photocatalytic performance of TiO_2. However, the exact role of CNTs in TiO_2/CNT composites is still poorly understood especially as it can be convoluted by factors such as synthesis methods, CNT morphologies, and

weight ratio of CNTs to TiO_2. Further insight into their syntheses and mechanisms is clearly required.

The conventional method for synthesizing TiO_2/CNT include sol-gel and hydrothermal processes [32]. Sol–gel synthesis utilizes inorganic metal salts or metal organic compounds to produce a sol, which transitions from a liquid to a gel upon polymerization of the precursor and loss of solvent. The hydrothermal method [33] used in this study involves heating a solution containing the titanium precursor to temperatures above the boiling point of the solvent, resulting in significantly increased pressures within the autoclave reactor. Synthesis parameters such as heating time in the autoclave, temperature, and pH affect the properties of resulting TiO_2 and offer a reliable path for improved control of the composite properties. Low temperature and relatively short reaction time proved best for synthesis of small TiO_2 particles, whereas mild acidity led to control of the crystal phase and yielded pure anatase [33, 34]. The hydrothermal method described earlier has been used by Zhang et al. [35] for creating TiO_2/CNT composites, whereas Jitianu et al. [36] showed TiO_2 decorations on MWCNTs were possible. Silva et al. [37] also showed that microwave-assisted hydrothermal process can be used for high mass loading of metal oxide and CNT composites. Hydrothermal synthesis of TiO_2/MWCNT composites was explored in this work due to the possibility of controlling the TiO_2 phase by controlling pH during the TiO_2 nucleation step in the hydrothermal aging process. To the best of our knowledge, no studies have been reported on the degradation of acetaldehyde, a common indoor pollutant [38, 39], using a hydrothermally prepared mesoporous CNT/TiO_2 photocatalyst. Moreover, whereas many studies involving TiO_2/CNT composites have focused on liquid-phase degradation of dyes, few have investigated gas-phase VOC degradation [40, 41].

In this work, a hydrothermal synthesis method has been used to synthesize TiO_2/MWCNT catalyst composites for efficient degradation of acetaldehyde under UV illumination. The hydrothermal method shows promise in controlling the anatase/rutile ratio, as well as producing diameter-controlled crystalline TiO_2 particles on a large scale [42]. Catalysts were synthesized with nominal mass ratios of 1:100 (TiO_2/MWCNT-1%), 1:20 (TiO_2/MWCNT-5%), and pure TiO_2 (100% TiO_2) as a reference. Performance of the composites was tested in the photocatalytic degradation of acetaldehyde in a batch reactor.

Results and discussion

Characterization of photocatalysts

XRD was used to characterize the phase composition of TiO_2 and TiO_2/MWCNT composites, and their diffraction patterns are presented in Fig. 1. The anatase peaks at 2θ values of 25.40°, 37.9°, 48.0°, 53.9°, and 55.1° can be indexed to (101), (004), (200), (105), and (211) crystal planes, respectively. Diffraction peaks for rutile at 27.4°, 36.2°, 41.3°, 54.4°, and 56.7° are present, which are indexed to (110), (101), (111), (211), and (220) crystal planes. The primary diffraction peak for brookite at 30.9°, indexed to (121), is also present. These peak assignments are also in agreement with prior studies [43, 44, 45, 46]. Comparing the reflection peaks observed in TiO_2 with the TiO_2/MWCNT composites, it can be concluded the dominant phase in all photocatalysts is anatase, although the TiO_2/MWCNT-5% composite appears to have a substantial fraction of rutile. A summary of the complete phase composition of the photocatalysts is presented in Table SI. The height ratio of the dominant anatase peak at 25.2° to the dominant rutile peak at 27.4° (I_{Ana}/I_{Rut}) can be used to determine the weight fraction of anatase and rutile crystalline phases of TiO_2 from Eq. (1) as demonstrated by Spurr and Myers [47]; the calculated mass ratios of anatase to rutile in TiO_2, TiO_2/MWCNT-1%, and TiO_2/MWCNT-5% are 66:34, 98:2, and 92:8, respectively. It is worth mentioning the characteristic peak of MWCNTs (002) located at $2\theta = 25°$ is not observed for the TiO_2/MWCNT samples. This is most likely due to the overlap with the strong anatase (101) reflections.

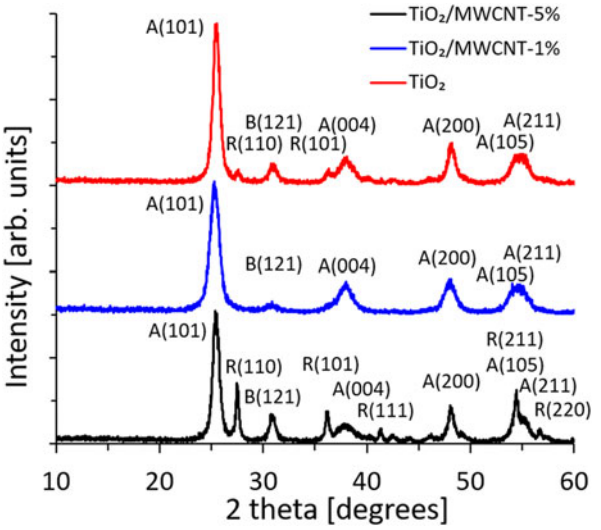

Figure 1: XRD patterns of TiO_2 and TiO_2–MWCNT nanocomposites. Peak labels have been included to correlate peaks to crystal phase [anatase (A), rutile (R), or brookite (B)].

$$f = \frac{1}{1 + 1.26\left(\frac{I_R}{I_A}\right)} \quad . \tag{1}$$

Average TiO_2 particle size for the samples (Table I) was calculated from the full width at half maximum (FWHM) of the principal anatase (101) peak at 25.2° using the Williamson–Hall method. Average TiO_2 particle sizes for TiO_2, TiO_2/

MWCNT-1%, and TiO_2/MWCNT-5% composites are 6.1, 5.8, and 7.2 nm, respectively. The high uniformity in TiO_2 particle sizes for the catalyst composites indicates the addition of MWCNTs during synthesis did not affect the size. Analysis of the E_g band (≈142 cm^{-1}) in the Raman spectra (Fig. S1) confirms the insignificant differences in particle size, as size discrepancies would manifest as an increase in peak frequency [48]. Scanning electron micrograph (SEM) images of the synthesized photocatalysts presented in Fig. 2 further illustrate the similarity of the bulk powder morphologies. Using energy-dispersive X-ray spectroscopy (EDX), carbon amounts were estimated at 1.4 and 6.6 wt% for TiO_2/MWCNT-1% and TiO_2/MWCNT-5% catalysts, respectively; these values indicate good agreement with the nominal values of 99 and 95 wt% TiO_2 in the samples. EDX data shown in Fig. 3 reveal TiO_2/MWCNT-5% contains pockets of carbon in different regions exceeding 10 wt%, which may indicate CNT clustering during the TiO_2 nucleation phase. Intimate contact between MWCNTs and TiO_2 is apparent in the transmission electron microscopic (TEM) images for TiO_2/MWCNT-5% in Fig. 4, even after 10 min of sonication during the sample preparation process for TEM characterization; this provides evidence of strong interactions between MWCNTs and TiO_2 nanoparticles, and high dispersion, especially for TiO_2/MWCNT-1%. Particle sizes estimated from the TEM images for the samples are in the range of 3–8 nm. The slight discrepancy in particle size obtained from TEM and XRD is consistent with overestimation of the size of crystallite particles by the Scherrer equation [49, 50].

TABLE I: Summary of catalyst properties.

Catalyst characterization			
	TiO_2	TiO_2/MWCNT-1%	TiO_2/MWCNT-5%
Surface area (m^2/g)[a]	74.6	141.6	68.2
Total pore volume (cm^3/g)[a]	0.14	0.30	0.16
Average pore diameter (nm)[a]	7.60	8.36	9.42
TiO_2 average diameter (nm)[b]	6.1	5.8	7.2
Anatase content (wt%)[b]	92	100	67
Carbon content (wt%)[c]	N/A	1.4	6.6

[a]Nitrogen physisorption.
[b]XRD.
[c]EDX.

Brunauer–Emmet–Teller (BET) surface areas of pure TiO_2, TiO_2/MWCNT-1%, and TiO_2/MWCNT-5% were determined to be 74.6, 141.6, and 68.2 m^2/g, respectively. The adsorption–desorption isotherms are presented in Fig. S2. The dramatic difference in surface area clearly indicates an effect of MWCNTs on the morphology of the photocatalysts, which could stem from the presence of MWCNTs during the nucleation of TiO_2 nanoparticles as part of the hydrothermal process. A small amount of MWCNTs (~1 wt%) effectively increased the surface area of resulting composites, whereas a further increase in the amount of MWCNTs (~5 wt%) resulted in particle agglomeration, reducing the overall surface

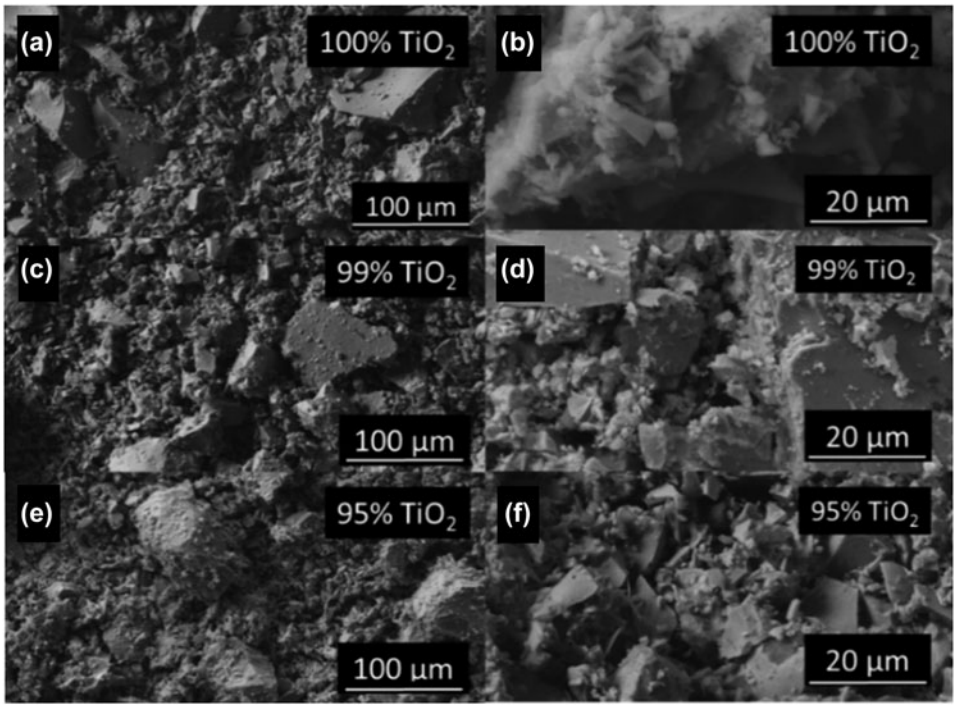

Figure 2: Low- and high-magnification SEM images of photocatalysts: TiO_2 (a, b), TiO_2/MWCNT-1% (c, d), and TiO_2/MWCNT-5% (e, f).

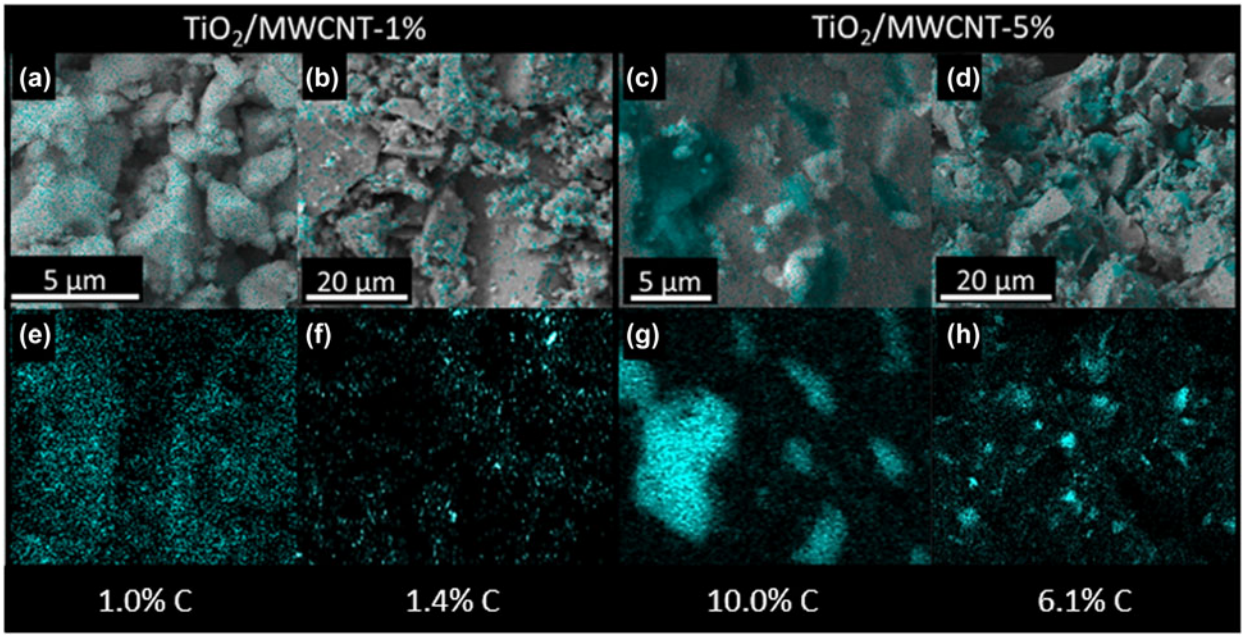

Figure 3: Carbon dispersion within photocatalysts. SEM images with EDS mapping of elemental carbon overlayed (a–d). EDS mapping of elemental carbon illustrating carbon dispersion.

area of the catalyst composite. Total pore volumes and average pore sizes determined by the Barrett–Joyner–Halenda (BJH) method for pure TiO_2, TiO_2/MWCNT-1%, and TiO_2/MWCNT-5% are summarized in Table I. The existence of mesopores in the catalyst composites is evidenced by pore sizes in the order 7.6, 8.4, and 9.4 nm for TiO_2, TiO_2/MWCNT-1%, and TiO_2/MWCNT-5%, respectively. Significant increase in porosity is observed in the TiO_2/MWCNT-1% composite, evidenced by substantially greater pore volume despite comparable pore size. Use of a hydrothermal method with a low weight fraction of MWCNTs yields TiO_2/MWCNT composites characterized by a combination of large specific surface area and pore size distributions in the mesopore range—features beneficial in catalysis.

X-ray photoelectron spectroscopic (XPS) characterization was performed to elucidate the surface composition of the photocatalysts. Figure 5 shows high-resolution XPS spectra for the O 1s region of photocatalysts fitted using two asymmetric peak components. The peak component at binding energy of ~531 eV is attributed to the oxygen bonded to Ti (Ti–O) in TiO_2, whereas the component at ~532 eV is related to the hydroxyl group [51]. Results of deconvolution of O 1*s* peak for the photocatalysts are summarized in Table II. Percentage concentrations of the two oxygen species identified changes with the amount of MWCNTs used during synthesis. Hydroxyl content in the photocatalysts decreases in the following order: TiO_2/MWCNT-1% > TiO_2/MWCNT-5% > TiO_2. This result suggests the presence of small amounts of MWCNTs (~1 wt%) enhances chemisorption of water on the surface of TiO_2—a feature hardly observed for composites with 5 wt%. Prior studies have shown chemisorption of water on TiO_2 composites is enhanced with the addition of CNTs [51, 52]. Since XPS analysis occurs under ultrahigh vacuum, the observed hydroxyl species is a result of chemisorption, not physisorption. XPS analysis of the catalyst composites reveals a substantially higher percentage of chemisorbed hydroxyl groups on the surface of the TiO_2/MWCNT-1%. Hydroxyl enrichment on the surface of TiO_2 promotes photocatalytic activity due to an increase in the generation of •OH radicals from the reaction between photogenerated holes and chemisorbed hydroxyl ions (or moisture) on the surface of photocatalyst. Therefore, synthesis approaches that yield high amounts of hydroxyl groups on the surface benefit photocatalytic reactions.

Photocatalytic activity

The activity of photocatalysts was measured by evaluating the rate of acetaldehyde degradation in the gas phase under UV light illumination. Figure 6 shows data for degradation of acetaldehyde over pure TiO_2, TiO_2/MWCNT-1% and TiO_2/MWCNT-5%. It is clear from the results that TiO_2/MWCNT-1% shows the highest photocatalytic performance because the rate of decrease of relative concentration (C/C_o) is the fastest among the photocatalysts [Fig. 6(a)]. Photocatalytic degradation of acetaldehyde is assumed to be a pseudo–first-order reaction [53] with the following simplified Langmuir–Hinshelwood kinetic model when initial concentration (C_o) is negligible:

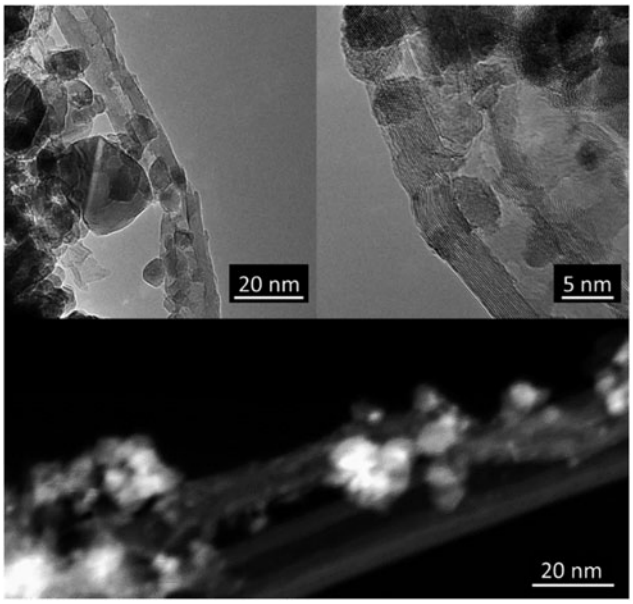

Figure 4: TEM images of TiO_2 particles on MWCNTs in the TiO_2/MWCNT-5% sample.

$$\ln\left(\frac{C}{C_o}\right) = -k_o t \quad , \tag{2}$$

where k_o is the apparent first-order rate constant. From the kinetic plots in Fig. 6(b), the TiO_2/MWCNT-1% shows the highest slope and, consequently, the highest average rate constant [Fig. 6(c)]. By contrast, composites prepared without MWCNTs (pure TiO_2), or with relatively high amounts of MWCNTs (TiO_2/MWCNT-5%), exhibit inferior photocatalytic performance. The respective shades around the plots in Fig. 6 show the range within one standard deviation for all data collected at each time interval. Projection lines intercept the *y*-axis after time zero due to desorption of acetaldehyde when the UV lights were switched on.

The average rate constant for acetaldehyde degradation with TiO_2 is 8.23×10^{-2} min^{-1}. In particular, degradation reactions with TiO_2/MWCNT-1% resulted in a photocatalytic rate constant of 15.0×10^{-2} min^{-1}, which is higher than that of a pure TiO_2 photocatalyst by almost a factor of two. By comparison, Sano et al. [54] saw a 60% increase in acetaldehyde degradation rate using a platinum-doped TiO_2 catalyst as compared with P25 in humid air, whereas Vijayan et al. [20] achieved a 40% increase in the reaction rate for acetaldehyde PCO under UV illumination with a titania nanotube/SWCNT composite. It is apparent introducing a small amount of MWCNTs into a TiO_2 matrix enhances the photocatalytic activity of the resulting TiO_2-based composites. Conversely, the rate constant obtained for the degradation reaction with TiO_2/MWCNT-5% is 6.50×10^{-2} min^{-1}, which is surprisingly lower than that of pure TiO_2; this indicates a further addition of MWCNTs, beyond the optimum loading ratio of 1:100 (MWCNTS:TiO_2), diminishes the effectiveness of the photocatalyst.

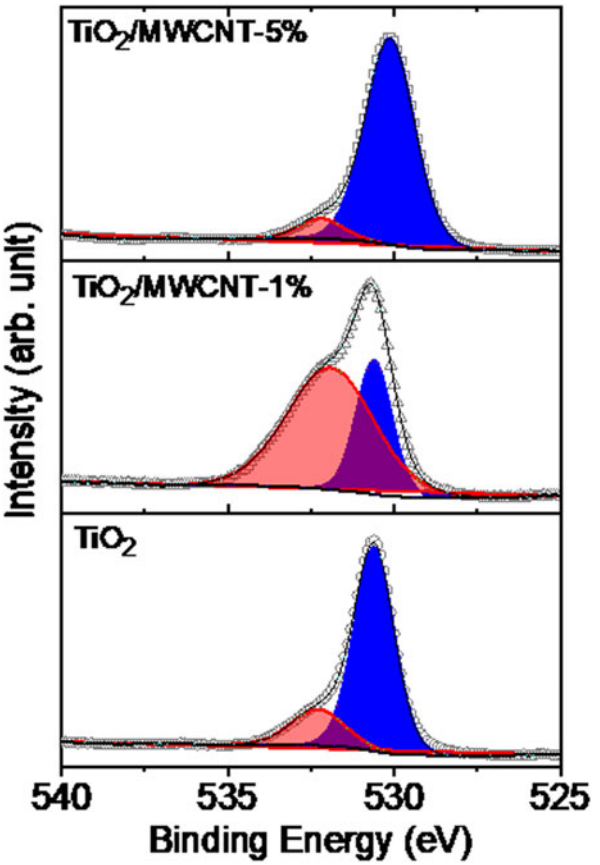

Figure 5: XPS high-resolution O 1*s* spectra of photocatalysts fitted using two asymmetric peak components.

As mentioned earlier, the TiO_2/MWCNT-5% catalyst is characterized by a lower percentage of anatase (~67 wt%). The observed difference in photocatalytic performance is not

TABLE II: Summary of results of deconvolution of high-resolution XPS O 1*s* spectra of TiO_2 and TiO_2/MWCNT composites using peak components with asymmetric line shapes.

Materials	O 1*s* (Ti–O)	O 1*s* (OH)
TiO_2		
Binding energy (eV)	530.1	532.2
Peak area	38941.7	3402.4
% Concentration	91.97	8.03
TiO_2/CNT-1%		
Binding energy (eV)	530.6	531.9
Peak area	10104.5	22672.0
% Concentration	30.84	69.16
TiO_2/CNT-5%		
Binding energy (eV)	530.6	532.3
Peak area	32081.9	7597.3
% Concentration	80.86	19.14

attributed to the composition of the crystal phases because the ideal ratio of anatase to rutile for maximal PCO rates has been shown to be between 40 and 80% anatase [55]. Electronic structure calculations for mixed rutile–anatase systems have revealed band alignment of rutile lies higher than that of anatase, resulting in hole accumulation in the valence band of rutile [56]. This conclusion supports the idea that higher rutile amounts than that in P25 may be beneficial to photocatalytic reactions that utilize holes generated in the valence band.

The TiO_2/MWCNT-1% composite is able to achieve 80% degradation of acetaldehyde after 110 min, whereas pristine TiO_2 achieves less than 60% degradation for the same illumination time. The primary mechanism for photocatalytic activity enhancement in TiO_2/MWCNT-1% is thought to be the result of structural effects from the addition of small amounts of MWCNTs. When higher amounts of MWCNTs are present, CNT agglomeration within the bulk catalyst occurs, resulting in TiO_2 nucleation around CNT bundles. This phenomenon is illustrated in Fig. 7. Whereas the average TiO_2 particle sizes are comparable, stark differences in surface area and pore volume suggest dispersion is affected by the presence of CNTs during TiO_2 particle nucleation. Without the presence of CNTs, TiO_2 particles experience some agglomeration during nucleation. Adding a small amount of MWCNTs (~1%) increased dispersion while providing nucleation sites for TiO_2 particle formation. Further addition of MWCNTs results in CNT clustering in the aqueous solution, due to their high hydrophobicity despite the oxidation of the MWCNTs. MWCNT clustering can be observed in both EDX (Fig. 3) and Raman spectroscopic results (Fig. S1). Raman spectra for the TiO_2/MWCNT-5% sample show substantial differences in intensity of the characteristic peaks of MWCNTs (i.e., the D-band ~1350 cm^{-1} and G-band ~1590 cm^{-1}) between the two spectra obtained from two different spots. The spectrum with carbon peaks of higher intensity exemplifies the agglomeration of CNTs in the scanned region.

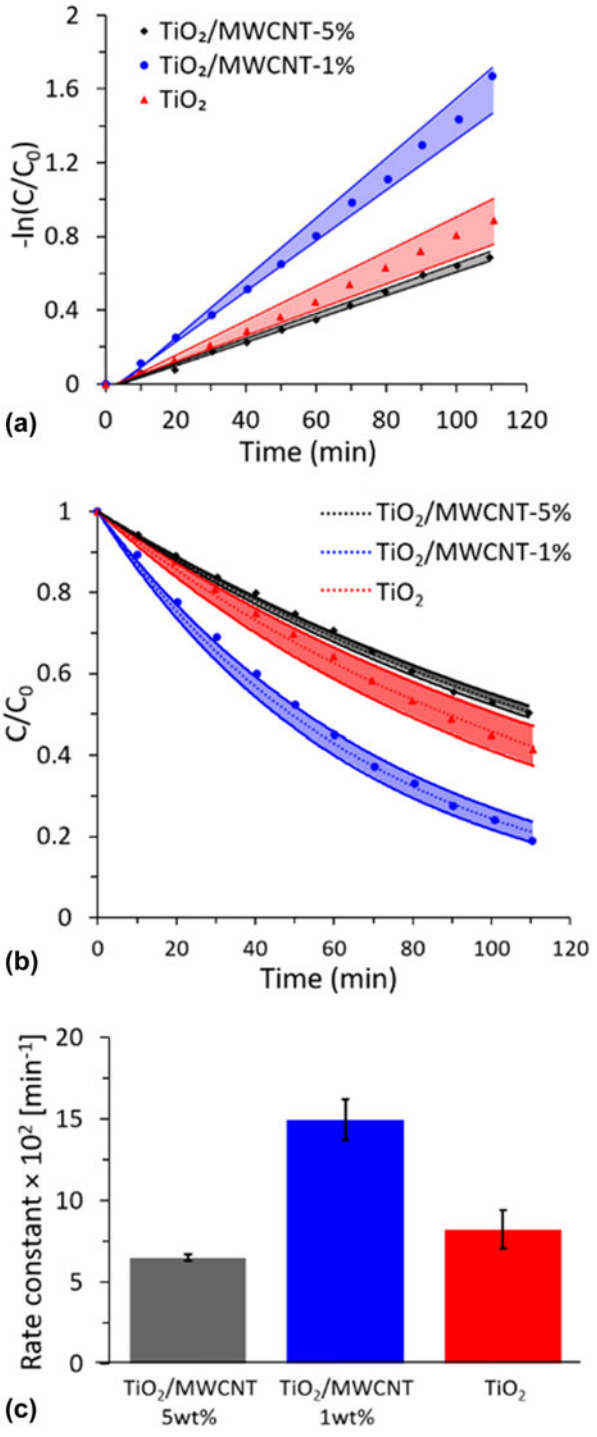

Figure 6: (a) Degradation curves of photocatalyst performance projection. Center lines indicate the first-order rate equation derived from the average degradation data for each catalyst. (b) Photocatalytic degradation of acetaldehyde as a function of UV illumination time. (c) Comparison of the average rate constants for the photocatalytic degradation of acetaldehyde using TiO_2, TiO_2/MWCNT-1%, and TiO_2/MWCNT-5%.

MWCNT clustering results in agglomeration of TiO_2 particles around the MWCNT bundles in addition to the typical nucleation and aggregation experienced in pristine

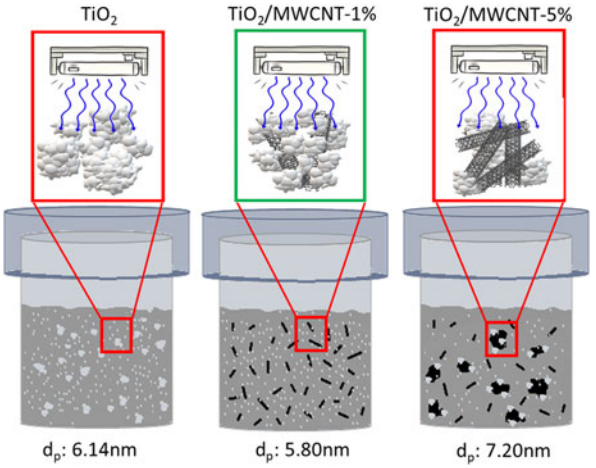

Figure 7: Proposed mechanism for the role of CNTs in TiO_2 nucleation and dispersion during hydrothermal synthesis of TiO_2/MWCNTs.

TiO_2 solution. As a consequence, the surface area and total pore volume of the photocatalyst decrease, resulting in a lower photocatalytic performance. In addition, CNT light absorption may begin to hinder the effectiveness of TiO_2 as the active photocatalytic material [57]. UV-vis diffuse reflectance spectroscopy (DRS) data provided in Fig. S3 confirm the photocatalytic activity enhancement in the TiO_2/MWCNT-1% catalyst is not due to band gap reduction as it appears to have blue-shifted subtly compared with the TiO_2 catalyst. These results support the hypothesis of photocatalytic enhancement from MWCNT addition due to physical effects.

Conclusions

CNT/TiO_2 catalysts of different CNT:TiO_2 ratios were synthesized using a hydrothermal method. The addition of only 1 wt% MWCNTs resulted in nearly double the degradation rate of acetaldehyde vapor. The observed catalytic enhancement is attributed to morphological differences caused by the presence of MWCNTs during TiO_2 particle nucleation and change in surface chemistry of the photocatalysts. The presence of small amounts of MWCNTs (~1 wt%) enhances chemisorption of water on the surface of TiO_2. Further addition of MWCNTs corresponding to 5 wt% resulted in lower photocatalytic performance, which is attributed to the agglomeration of CNTs during the hydrothermal process and possible reduction, as well as interference in the absorption of light by TiO_2.

Experimental

Chemicals

MWCNTs (purity >95%, outer diameter 20–30 nm, and length 10–30 μm) were obtained from Chengdu Organic Chemicals Co., Ltd., Hydrogen peroxide (30%) was obtained from Fisher Scientific. Titanium tetrachloride ($TiCl_4$, purity >99.0%) was obtained from Strem Chemicals. Sodium hydroxide (NaOH, purity >99%) and acetaldehyde (C_2H_4O, purity >99%) were obtained from Sigma-Aldrich. Dry air was obtained from Matheson.

CNT oxidation

MWCNTs were photo-oxidized in 30 wt% H_2O_2 via UV illumination (White-Rodger Comfort Plus UV200, 2 Philips TUV PL-L 60 W bulbs). UV-assisted H_2O_2 oxidation of MWCNTs has been shown to be effective and less aggressive in comparison to conventional acid oxidation using HNO_3 [58, 59]. In a typical batch, 0.5 g of MWCNTs were added to 200 mL of H_2O_2, which was maintained at 60 °C under UV illumination and vigorous stirring. The MWCNTs were oxidized for 72 h, with 50 mL of H_2O_2 being added at 24 and 48 h to sustain the process. After 72 h, the oxidized MWCNTs were removed from solution via vacuum filtration and rinsed with distilled water. Oxidized MWCNTs were obtained after the samples were vacuum-dried overnight at 60 °C.

Catalyst synthesis

Oxidized MWCNTs were dispersed in 50 mL H_2O via sonication at room temperature for 3 h. Following sonication, $TiCl_4$ amounts corresponding to TiO_2:MWCNT ratios of 99:1 and 95:5 were added dropwise at a rate of 1 mL/min, to the dispersed MWCNTs at ~5 °C under moderate stirring (0.88 mol/L Ti). After addition of the $TiCl_4$ and resulting exothermic reaction, the solution was allowed to cool from ~25 to 10 °C under continuous stirring. Once the solution reached 10 °C, 35 mL of 5 M NaOH were added to the solution to obtain a pH of 3–5. The addition of the strong base led to the formation of abundant NaCl, causing the solution to become highly viscous. The stir rate was increased gradually from 300 to 800 rpm as the viscosity increased. When the solution reached a pH range of 3–5, water was added under constant stirring to produce a solution of 0.44 mol/L Ti. The solution was then put in a steel autoclave and heated in the oven for 3 h at 150 °C, removed, and allowed to cool for 3 h. The TiO_2/MWCNT composite was dried by air continuously flowing over it for 24 h followed by 3 h in the oven at 80 °C. Once dried, TiO_2/MWCNT was crushed into a fine powder and baked at 250 °C for 3 h. To remove NaCl, the composite was rinsed via vacuum filtration with 250 mL of deionized water and allowed to dry for 12 h. Finally, the composite was calcined at 450 °C for 3 h (a temperature low enough to prevent TiO_2 sintering) [60], cooled, and stored as a powder. Before evaluation of the catalyst performance, the powders were sieved to <125 μm to reduce particle agglomeration and grain size distribution.

Photocatalysts were synthesized with nominal mass ratios of 1:100 (TiO_2/MWCNT-1%), 1:20 (TiO_2/MWCNT-5%), and pure TiO_2 (100% TiO_2) as a reference.

Characterization

XRD patterns were obtained using a Rigaku MiniFlex II diffractometer with a Cu K_α radiation source. Two theta scanning angles from 10° to 80° degrees were taken with a step size of 0.02° and scan speed of 2.0°/min for all photocatalysts. Surface area and pore volume were derived from N_2 adsorption–desorption measurements at −196 °C. The BET method [61] was applied to the adsorption isotherm in the relative pressure range of 0.02–0.35 to calculate the specific surface area of the synthesized photocatalysts. Pore-size distribution was obtained from the desorption branch at a relative pressure of 0.99 of the isotherm using the BJH model [62]. SEM were obtained using a Hitachi S5200, operated at 10 kV and equipped with EDX. TEM images were obtained with an FEI Tecnai F20 XT equipped with EDX at 120 kV. A small amount of photocatalyst powder was dispersed in ethanol by sonication for 10 min, and a drop of the solution was deposited onto a carbon TEM grid. Raman spectroscopy was obtained from a Renishaw Raman spectrometer using a CW laser with a wavelength of 514 nm. Raman spectra were collected at different locations of the sample. The TiO_2 and TiO_2/MWCNT samples were analyzed by UV-visible diffuse reflectance spectroscopy (UV-vis DRS) using a Shimadzu UV-2600 spectrometer with $BaSO_4$ as the background material. XPS measurements were conducted on a Kratos Ultra XPS system with a standard Mg K_α source ($h\nu$ = 1253.6 eV). A charge neutralizer was employed to minimize the effect of charging. High-resolution spectra were acquired at 20 eV pass energy with 0.1 eV steps. XPS spectra were analyzed using CasaXPS software. Peak components in the high-resolution spectra were fit with a combination of Gaussian and Lorentzian peak shapes.

Photocatalytic performance

In a standard catalyst evaluation, 0.100 ± 0.001 g of sieved photocatalyst powder was loaded into a borosilicate sample dish, which was then placed in a 750-mL borosilicate batch reactor. The reactor was purged using UHP air (low CO_2 and H_2O content) at 6 liters per minute (LPM) for 5 min. Thereafter, acetaldehyde vapor corresponding to 1000 ppmv was injected into the reactor and allowed to equilibrate in darkness for 90 min. The ultraviolet illumination system—consisting of two 25 W Sylvania 21703 (356 nm) bulbs and two 13 W ReptiSun 10.0 UV/B bulbs (emission spectrum displayed in Fig. S1)—was switched on to initiate the reaction for a duration of 120 min. One-mL gas samples were taken from the reactor at ~10 min intervals for analysis. The decrease in acetaldehyde concentration and increase in CO_2 concentration were monitored using an SRI 310C gas chromatograph equipped with a Restek silica gel column (8046-895, 6 ft length, 2 mm ID), flame ionization detector (FID), and on-column injection. Detected peaks were integrated using PeakSimple Chromatography Integration software. The relative concentration is expressed as C/C_o, where C is the concentration of acetaldehyde at time t and C_o is the initial acetaldehyde concentration. The photocatalytic experiment was conducted at room temperature (~25 °C) with an indoor relative humidity of ~50%. The photocatalytic performance of three separate 0.100 g samples from each composite ratio were tested to ensure statistical significance of the results. Average catalyst performance was calculated using the average concentration of three degradation experiments for each catalyst. First-order rate assumptions were applied in analysis of the degradation data.

Acknowledgment

This work was supported by the National Science Foundation (Grant No. 1653527).

Supplementary material

To view supplementary material for this article, please visit https://doi.org/10.1557/jmr.2020.97.

References

1. **A. Fujishima and K. Honda**: Electrochemical photolysis of water at a semiconductor electrode. *Nature* **238**, 37–38 (1972).
2. **M.R. Hoffmann, S.T. Martin, W. Choi, and D.W. Bahnemann**: Environmental applications of semiconductor photocatalysis. *Chem. Rev.* **95**, 69–96 (1995).
3. **T. Kjellstrom, M. Lodh, T. McMichael, G. Ranmuthugala, R. Shrestha, and S. Kingsland: Air and water pollution:** Burden and strategies for control. In *Disease Control Priorities in Developing Countries*, 2nd ed., D.T. Jamison, J.G. Breman, A.R. Measham, G. Alleyne, M. Claeson, D.B. Evans, P. Jha, A. Mills, and P. Musgrove, eds. (Washington (DC), Oxford University Press, 2006); pp. 817–832.
4. **P.B. Amama, K. Itoh, and M. Murabayashi**: Photocatalytic oxidation of trichloroethylene in humidified atmosphere. *J. Mol. Catal. A: Chem.* **176**, 165–172 (2001).
5. **P.B. Amama, K. Itoh, and M. Murabayashi**: Gas-phase photocatalytic degradation of trichloroethylene on pretreated TiO_2. *Appl. Catal., B* **37**, 321–330 (2002).
6. **P.B. Amama, K. Itoh, and M. Murabayashi**: Photocatalytic degradation of trichloroethylene in dry and humid atmospheres: Role of gas-phase reactions. *J. Mol. Catal. A: Chem.* **217**, 109–115 (2004).

7. **P.B. Amama, K. Itoh, and M. Murabayashi**: Effect of RuO_2 deposition on the activity of TiO_2: Photocatalytic oxidation of trichloroethylene in aqueous phase. *J. Mater. Sci.* **39**, 4349–4351 (2004).
8. **D. Huang, S. Liao, S. Quan, L. Liu, Z. He, J. Wan, and W. Zhou**: Preparation and characterization of anatase N–F-codoped TiO_2 sol and its photocatalytic degradation for formaldehyde. *J. Mater. Res.* **22**, 2389–2397 (2007).
9. **A.H.C. Chan, J.F. Porter, J.P. Barford, and C.K. Chan**: Effect of thermal treatment on the photocatalytic activity of TiO_2 coatings for photocatalytic oxidation of benzoic acid. *J. Mater. Res.* **17**, 1758–1765 (2002).
10. **J. Wen, X. Li, W. Liu, Y. Fang, J. Xie, and Y. Xu**: Photocatalysis fundamentals and surface modification of TiO_2 nanomaterials. *Chin. J. Catal.* **36**, 2049–2070 (2015).
11. **A. Fujishima, T.N. Rao, and D.A. Tryk**: Titanium dioxide photocatalysis. *J. Photochem. Photobiol., C* **1**, 1–21 (2000).
12. **M. Trépanier, A.K. Dalai, and N. Abatzoglou**: Synthesis of CNT-supported cobalt nanoparticle catalysts using a microemulsion technique: Role of nanoparticle size on reducibility, activity and selectivity in Fischer–Tropsch reactions. *Appl. Catal., A* **374**, 79–86 (2010).
13. **B. Prasai, B. Cai, M.K. Underwood, J.P. Lewis, and D.A. Drabold**: Properties of amorphous and crystalline titanium dioxide from first principles. *J. Mater. Sci.* **47**, 7515–7521 (2012).
14. **J.E. Frederick, H.E. Snell, and E.K. Haywood**: Solar ultraviolet radiation at the earth's surface. *Photochem. Photobiol.* **50**, 443–450 (1989).
15. **A. Heller**: Conversion of sunlight into electrical power and photoassisted electrolysis of water in photoelectrochemical cells. *Acc. Chem. Res.* **14**, 154–162 (1981).
16. **A.J. Cowan, J. Tang, W. Leng, J.R. Durrant, and D.R. Klug**: Water splitting by nanocrystalline TiO_2 in a complete photoelectrochemical cell exhibits efficiencies limited by charge recombination. *J. Phys. Chem. C* **114**, 4208–4214 (2010).
17. **R. Asahi, T. Morikawa, T. Ohwaki, K. Aoki, and Y. Taga**: Visible-light photocatalysis in nitrogen-doped titanium oxides. *Science* **293**, 269–271 (2001).
18. **Y. Wang, Y. Wang, Y. Meng, H. Ding, Y. Shan, X. Zhao, and X. Tang**: A highly efficient visible-light-activated photocatalyst based on bismuth- and sulfur-codoped TiO_2. *J. Phys. Chem. C* **112**, 6620–6626 (2008).
19. **Y. Gai, J. Li, S-S. Li, J-B. Xia, and S-H. Wei**: Design of narrow-gap TiO_2: A passivated codoping approach for enhanced photoelectrochemical activity. *Phys. Rev. Lett.* **102**, 036402 (2009).
20. **B.K. Vijayan, N.M. Dimitrijevic, D. Finkelstein-Shapiro, J. Wu, and K.A. Gray**: Coupling titania nanotubes and carbon nanotubes to create photocatalytic nanocomposites. *ACS Catal.* **2**, 223–229 (2012).
21. **K. Woan, G. Pyrgiotakis, and W. Sigmund**: Photocatalytic carbon-nanotube–TiO_2 composites. *Adv. Mater.* **21**, 2233–2239 (2009).
22. **G. An, W. Ma, Z. Sun, Z. Liu, B. Han, S. Miao, Z. Miao, and K. Ding**: Preparation of titania/carbon nanotube composites using supercritical ethanol and their photocatalytic activity for phenol degradation under visible light irradiation. *Carbon* **45**, 1795–1801 (2007).
23. **C.G. Silva and J.L. Faria**: Photocatalytic oxidation of benzene derivatives in aqueous suspensions: Synergic effect induced by the introduction of carbon nanotubes in a TiO_2 matrix. *Appl. Catal., B* **101**, 81–89 (2010).
24. **N. Li, Y. Ma, B. Wang, Y. Huang, Y. Wu, X. Yang, and Y. Chen**: Synthesis of semiconducting SWNTs by arc discharge and their enhancement of water splitting performance with TiO_2 photocatalyst. *Carbon* **49**, 5132–5141 (2011).
25. **W-D. Zhang, B. Xu, and L-C. Jiang**: Functional hybrid materials based on carbon nanotubes and metal oxides. *J. Mater. Chem.* **20**, 6383–6391 (2010).
26. **L-L. Tan, W-J. Ong, S-P. Chai, and A. Mohamed**: Reduced graphene oxide-TiO_2 nanocomposite as a promising visible-light-active photocatalyst for the conversion of carbon dioxide. *Nanoscale Res. Lett.* **8**, 1–9 (2013).
27. **Y. Long, Y. Lu, Y. Huang, Y. Peng, Y. Lu, S-Z. Kang, and J. Mu**: Effect of C_{60} on the photocatalytic activity of TiO_2 nanorods. *J. Phys. Chem. C* **113**, 13899–13905 (2009).
28. **J. Yu, T. Ma, G. Liu, and B. Cheng**: Enhanced photocatalytic activity of bimodal mesoporous titania powders by C_{60} modification. *Dalton Trans.* **40**, 6635–6644 (2011).
29. **G. Jiang, Z. Lin, C. Chen, L. Zhu, Q. Chang, N. Wang, W. Wei, and H. Tang**: TiO_2 nanoparticles assembled on graphene oxide nanosheets with high photocatalytic activity for removal of pollutants. *Carbon* **49**, 2693–2701 (2011).
30. **Q. Xiang, J. Yu, and M. Jaroniec**: Preparation and enhanced visible-light photocatalytic H_2-production activity of graphene/C_3N_4 composites. *J. Phys. Chem. C* **115**, 7355–7363 (2011).
31. **W. Fan, Q. Lai, Q. Zhang, and Y. Wang**: Nanocomposites of TiO_2 and reduced graphene oxide as efficient photocatalysts for hydrogen evolution. *J. Phys. Chem. C* **115**, 10694–10701 (2011).
32. **C-C. Wang and J.Y. Ying**: Sol–gel synthesis and hydrothermal processing of anatase and rutile titania nanocrystals. *Chem. Mater.* **11**, 3113–3120 (1999).
33. **H. Cheng, J. Ma, Z. Zhao, and L. Qi**: Hydrothermal preparation of uniform nanosize rutile and anatase particles. *Chem. Mater.* **7**, 663–671 (1995).
34. **V.O. Kotsyubynsky, I.F. Myronyuk, L.I. Myronyuk, V.L. Chelyadyn, M.H. Mizilevska, A.B. Hrubiak, O.K. Tadeush, and F.M. Nizamutdinov**: The effect of pH on the nucleation of titania by hydrolysis of $TiCl_4$. *Mater. Werkst.* **47**, 288–294 (2016).
35. **B. Zhang, R. Shi, Y. Zhang, and C. Pan**: CNTs/TiO_2 composites and its electrochemical properties after UV light irradiation. *Prog. Nat. Sci.: Mater. Int.* **23**, 164–169 (2013).
36. **A. Jitianu, T. Cacciaguerra, R. Benoit, S. Delpeux, F. Béguin, and S. Bonnamy**: Synthesis and characterization of carbon nanotubes–TiO_2 nanocomposites. *Carbon* **42**, 1147–1151 (2004).

37. **R.M. Silva, B.S. Noremberg, N.H. Marins, J. Milne, I. Zhitomirsky, and N.L.V. Carreño**: Microwave-assisted hydrothermal synthesis and electrochemical characterization of niobium pentoxide/carbon nanotubes composites. *J. Mater. Res.* **34**, 592–599 (2019).
38. **M. Hulin, D. Caillaud, and I. Annesi-Maesano**: Indoor air pollution and childhood asthma: Variations between urban and rural areas. *Indoor Air* **20**, 502–514 (2010).
39. **C. Marchand, B. Bulliot, S. Le Calvé, and P. Mirabel**: Aldehyde measurements in indoor environments in Strasbourg (France). *Atmos. Environ.* **40**, 1336–1345 (2006).
40. **T. An, J. Chen, X. Nie, G. Li, H. Zhang, X. Liu, and H. Zhao**: Synthesis of carbon nanotube–anatase TiO_2 sub-micrometer-sized sphere composite photocatalyst for synergistic degradation of gaseous styrene. *ACS Appl. Mater. Interfaces* **4**, 5988–5996 (2012).
41. **J. Chen, G. Li, Y. Huang, H. Zhang, H. Zhao, and T. An**: Optimization synthesis of carbon nanotubes-anatase TiO_2 composite photocatalyst by response surface methodology for photocatalytic degradation of gaseous styrene. *Appl. Catal., B* **123–124**, 69–77 (2012).
42. **W.L. Suchanek and R.E. Riman**: Hydrothermal synthesis of advanced ceramic powders. *Adv. Sci. Technol.* **45**, 184–193 (2006).
43. **B.K. Mutuma, G.N. Shao, W.D. Kim, and H.T. Kim**: Sol–gel synthesis of mesoporous anatase–brookite and anatase–brookite–rutile TiO_2 nanoparticles and their photocatalytic properties. *J. Colloid Interf. Sci.* **442**, 1–7 (2015).
44. **Y. Zhang, Z-R. Tang, X. Fu, and Y-J. Xu**: TiO_2–graphene nanocomposites for gas-phase photocatalytic degradation of volatile aromatic pollutant: Is TiO_2–graphene truly different from other TiO_2–carbon composite materials? *ACS Nano* **4**, 7303–7314 (2010).
45. **X-H. Xia, Z-J. Jia, Y. Yu, Y. Liang, Z. Wang, and L-L. Ma**: Preparation of multi-walled carbon nanotube supported TiO_2 and its photocatalytic activity in the reduction of CO_2 with H_2O. *Carbon* **45**, 717–721 (2007).
46. **Y. Zhu, T. Liu, and C. Ding**: Structural characterization of TiO_2 ultrafine particles. *J. Mater. Res.* **14**, 442–446 (1999).
47. **R.A. Spurr and H. Myers**: Quantitative analysis of anatase-rutile mixtures with an X-ray diffractometer. *Anal. Chem.* **29**, 760–762 (1957).
48. **C. Papo, Z. Tetana, P. Franklyn, and S. Mhlanga**: Synthesis and study of carbon/TiO_2 and carbon/TiO_2 core–shell micro-/nanospheres with increased density. *J. Mater. Res.* **28**, 440–448 (2013).
49. **A.Y. Khodakov, W. Chu, and P. Fongarland**: Advances in the development of novel cobalt Fischer–Tropsch catalysts for synthesis of long-chain hydrocarbons and clean fuels. *Chem. Rev.* **107**, 1692–1744 (2007).
50. **J. Li, Y. Xu, D. Wu, and Y. Sun**: Hollow mesoporous silica sphere supported cobalt catalysts for F–T synthesis. *Catal. Today* **148**, 148–152 (2009).
51. **Y. Yu, J.C. Yu, C-Y. Chan, Y-K. Che, J-C. Zhao, L. Ding, W-K. Ge, and P-K. Wong**: Enhancement of adsorption and photocatalytic activity of TiO_2 by using carbon nanotubes for the treatment of azo dye. *Appl. Catal., B* **61**, 1–11 (2005).
52. **J. Yu, J.C. Yu, W. Ho, and Z. Jiang**: Effects of calcination temperature on the photocatalytic activity and photo-induced super-hydrophilicity of mesoporous TiO_2 thin films. *New J. Chem.* **26**, 607–613 (2002).
53. **I. Sopyan, M. Watanabe, S. Murasawa, K. Hashimoto, and A. Fujishima**: An efficient TiO_2 thin-film photocatalyst: Photocatalytic properties in gas-phase acetaldehyde degradation. *J. Photochem. Photobiol., A* **98**, 79–86 (1996).
54. **T. Sano, N. Negishi, K. Uchino, J. Tanaka, S. Matsuzawa, and K. Takeuchi**: Photocatalytic degradation of gaseous acetaldehyde on TiO_2 with photodeposited metals and metal oxides. *J. Photochem. Photobiol., A* **160**, 93–98 (2003).
55. **R. Su, R. Bechstein, L. So, R.T. Vang, M. Sillassen, B. Esbjornsson, A. Palmqvist, and F. Besenbacher**: How the anatase-to-rutile ratio influences the photoreactivity of TiO_2. *J. Phys. Chem. C* **115**, 24287–24292 (2011).
56. **P. Deak, B. Aradi, and T. Frauenheim**: Band lineup and charge carrier separation in mixed rutile-anatase systems. *J. Phys. Chem. C* **115**, 3443–3446 (2011).
57. **Y. Yu, J.C. Yu, J-G. Yu, Y-C. Kwok, Y-K. Che, J-C. Zhao, L. Ding, W-K. Ge, and P-K. Wong**: Enhancement of photocatalytic activity of mesoporous TiO_2 by using carbon nanotubes. *Appl. Catal., A* **289**, 186–196 (2005).
58. **B. Czecha, P. Oleszczuka, and A. Wiącek**: Advanced oxidation (H_2O_2 and/or UV) of functionalized carbon nanotubes (CNT–OH and CNT–COOH) and its influence on the stabilization of CNTs in water and tannic acid solution. *Environ. Pollut.* **200**, 161–167 (2015).
59. **H. Almkhelfe, X. Li, P. Thapa, K.L. Hohn, and P.B. Amama**: Carbon nanotube-supported catalysts prepared by a modified photo-Fenton process for Fischer–Tropsch synthesis. *J. Catal.* **361**, 278–289 (2018).
60. **H. Hahn, J. Logas, and R.S. Averback**: Sintering characteristics of nanocrystalline TiO_2. *J. Mater. Res.* **5**, 609–614 (1990).
61. **S. Brunauer, P.H. Emmett, and E. Teller**: Adsorption of gases in multimolecular layers. *J. Am. Chem. Soc.* **60**, 309–319 (1938).
62. **E.P. Barrett, L.G. Joyner, and P.P. Halenda**: The determination of pore volume and area distributions in porous substances. I. Computations from nitrogen isotherms. *J. Am. Chem. Soc.* **73**, 373–380 (1951).